minerals

Article

Prediction of Lithium Oilfield Brines Based on Seismic Data: A Case Study from L Area, Northeastern Sichuan Basin, China

Yuxuan Zhou [1,2], Yuyong Yang [1,2,*], Zhengyang Wang [1,2], Bing Zhang [1,2], Huailai Zhou [1,2] and Yuanjun Wang [1,3]

1 Key Lab of Earth Exploration & Information Techniques of Ministry of Education, Chengdu University of Technology, Chengdu 610059, China; zhouyuxuan_cdut@163.com (Y.Z.); wangzhengyang@stu.cdut.edu.cn (Z.W.); zhangb@cdut.edu.cn (B.Z.); zhouhuailai06@cdut.cn (H.Z.); wyj@cdut.edu.cn (Y.W.)
2 College of Geophysics, Chengdu University of Technology, Chengdu 610059, China
3 School of Education, China West Normal University, Nanchong 637002, China
* Correspondence: yangyuyong19@cdut.edu.cn

Abstract: Lithium is an important mineral resource and a critical element in the production of lithium batteries, which are currently in high demand. Oilfield brine has significant value as a raw material for lithium extraction. However, it is often considered a byproduct of oil and gas production and is either abandoned or reinjected underground. Exploration and development of oilfield brines can enhance the economic benefits of oilfields and avoid wasting resources. Current methods for predicting brine distribution rely on geological genetic analysis, which results in low accuracy and reliability. To address this issue, we propose a workflow for lithium brine prediction that uses seismic and logging data. We introduced waveform clustering control and used the mapping relationship between seismic waveforms and well-logging curves to predict high-quality reservoirs based on the electrical and physical properties of lithium brine reservoirs. In this workflow, the seismic waveforms were first clustered using singular value decomposition. The sample sets of well-logging properties were established for the target location. The target properties were divided into high- and low-frequency components and predicted separately. The predicted results of the high-quality reservoirs in the study area were verified using elemental content test results to demonstrate the effectiveness of the method. Our study indicates that well-logging property prediction constrained by waveform clustering can predict lithium brines in a carbonate reservoir.

Keywords: oilfield brine; waveform clustering; inversion; carbonate

check for updates

Citation: Zhou, Y.; Yang, Y.; Wang, Z.; Zhang, B.; Zhou, H.; Wang, Y. Prediction of Lithium Oilfield Brines Based on Seismic Data: A Case Study from L Area, Northeastern Sichuan Basin, China. *Minerals* **2024**, *14*, 159. https://doi.org/10.3390/min14020159

Academic Editors: Yun Wang, Shoudong Huo, Guofeng Liu, Zhengyong Ren and Michael S. Zhdanov

Received: 25 December 2023
Revised: 22 January 2024
Accepted: 27 January 2024
Published: 31 January 2024

1. Introduction

Lithium has attracted much attention in the 21st century as a new energy source or strategic resource (He et al., 2020) [1] and has been listed as a critical or near-critical element in several recent studies (Bradley et al., 2016; Cabello, 2021; He et al., 2020) [1–3]. Its significance is further magnified considering advancements in lithium battery technology and its utilization in controlled nuclear fusion. The metal Li has been identified as a promising anode material for next-generation Li-based batteries (Liu et al., 2022) [4]. A sustained annual growth rate of 7%–11% in the global demand for lithium resources has been recorded in recent years (Gil-Alana and Monge, 2019) [5]. Lithium resources are predominantly found in brine and granitic pegmatite deposits (Kesler et al., 2012) [6], accounting for 87% of the global lithium resources (Christmann et al., 2015; Gil-Alana and Monge, 2019) [5,7]. China has abundant lithium brine resources, with its reserves ranking third globally, after Bolivia and Chile, comprising approximately 30% of the world's total reserves (He et al., 2020) [1].

Brines are categorized into three types: geothermal, continental, and oilfield brines (Meng et al., 2021) [8]. Oilfield brine, a byproduct of petroleum development, is easier to obtain (Li et al., 2019) [9] and has a more stable chemical composition (Gong et al.,

2020) [10] than continental and geothermal brines. However, because oilfield brine is often regarded as waste, large amounts are directly discharged or stored, resulting in a waste of resources and environmental pollution (Al-Thukair et al., 2013) [11]. The detection and development of lithium oilfield brines can help convert them into valuable resources, which is significant for improving energy utilization efficiency and reducing environmental pollution (Moosavi et al., 2020) [12]. Owing to the active oil and gas development activities in the Sichuan Basin (Yang et al., 2018; Yi et al., 2019) [13,14], the total production of oilfield brine is increasing. Lithium resources from the oilfield brines in this basin have potential for development. Lithium oilfield brine reservoirs in the Sichuan Basin are generally developed in dolomites (Wen et al., 2014; Ni et al., 2018) [15,16]. Furthermore, because of the reef-flat sedimentary environment and multiple stages of dolomitization, the reservoirs exhibit rapid lateral changes (Zhao et al., 2011) [17]. Therefore, high-resolution methods are required for accurate reservoir prediction.

Numerous methods are currently used for predicting oilfield brine. These methods can be grouped into two categories. The first includes indirect exploration methods based on geological genesis. These methods use factors such as oilfield geological structures, sedimentary environments, and groundwater movement to predict the content, composition, and distribution of brine in oilfields (Araoka et al., 2014; Orberger et al., 2015; Zhang et al., 2022) [18–20]. The basic principle is to predict the sources, evolutionary processes, and hydrogeological characteristics of oilfield brines with a comprehensive analysis of the geological characteristics, genesis, and evolution of oil and gas reservoirs (Yu X. C. et al., 2022) [21]. These methods require geological prediction models and data; however, due to the limitations in obtaining data from wells, achieving reliable results in areas with few wells is difficult. Additionally, the distribution of brine between wells cannot be predicted directly. The second category involves direct exploration methods that use geophysical data. Currently, electrical exploration is the primary method used. Based on the large difference in electrical properties between brine layers and surrounding rocks (brine rock layers have low electrical resistivity) and the spatial patterns of electrical resistivity, the distribution of oilfield brine was successfully predicted (Jiao et al., 2005) [22]. However, this method has a low resolution and limited exploration depth, making detecting brines in deep oilfields difficult. Additionally, a combination of seismic and well-logging methods has been used to predict oilfield brines based on their acoustic characteristics (Yan et al., 2013; Huang et al., 2014) [23,24]. Based on a neural network method, a relationship between resistivity and seismic attributes was established and used to obtain resistivity information from seismic data to identify brine reservoirs (Hou et al., 2022) [25]. However, these methods utilize only the acoustic or electrical characteristics of the brine reservoir, thus resulting in high ambiguity.

With increasing exploration and development activities, an increasing number of reservoir prediction methods have been proposed (Smith et al., 2009; Ruiz and Cheng, 2010; Lu et al., 2016; Yang et al., 2022) [26–29]. By combining seismic and logging data and using different rock physics models, it is possible to estimate the elastic information of a target reservoir and predict the distribution of oil, gas, and water (Khoshdel et al., 2022) [30]. In general, petrophysical parameters (such as porosity and fluid saturation) can be predicted from elastic parameters using different rock physics models, such as sandstone (Keys and Xu, 2002; Mavko et al., 2009; Dvorkin and Nur, 1996) [31–33], shale (Ruiz and Azizo, 2011) [34], carbonate (Xu and White, 1995; Xu and Payne, 2009) [35,36], and fracture (Schoenberg and Sayers, 1995; Bakulin et al., 2000) [37,38] reservoir models. Elastic parameters are commonly obtained with seismic inversion, which uses elastic information contained in seismic waves. Common inversion methods include model-based (Cooke and Schneider, 1983; Russell and Hampson, 1991; Kumar et al., 2016) [39–41], prestack elastic (Aki and Richards, 1980; Zong et al., 2012, 2017; Lu et al., 2015, 2018) [42–46], nonlinear (neural networks and support vector machines) (Liu and Liu, 1998; Torresa et al., 2013; Cheng and Fu, 2022) [47–49], and geological statistical (Wu et al., 2008; Giroud et al., 2017; Mosser et al., 2020) [50–52] inversion. Model-based inversion has low lateral resolution and is unsuitable for reservoirs with rapid lateral changes (Yao and Gan, 2000) [53]. Prestack elastic inversion has resolution limitations within the seismic resolution range (Yin et al., 2014) [54]. Nonlinear inversion has strong multi-solution characteristics and lacks geological constraints. Geological statistical inversion results typically exhibit strong randomness in situations with few wells. Furthermore, when non-elastic parameters, such as resistivity and natural gamma, are required to predict reservoir properties, it is difficult to implement an inversion process by establishing an objective function.

It is a feasible strategy to predict electrical parameters using the elastic parameters obtained with inversion. Currently, several models can describe the relationship between elastic and electrical parameters (Pan et al., 2019) [55]; however, these models do not consider the presence of water, making their application in predicting oilfield brine reservoirs difficult. Seismic meme inversion (SMI), a high-resolution seismic inversion method (Yu Z. C. et al., 2023) [56], can improve both the vertical and horizontal resolutions of inversion results by establishing a mapping relationship between the seismic waveform and high-frequency well-logging curve. This method constructs Bayesian inversion frameworks for different seismic facies types to achieve facies-controlled inversion. Chen et al. (2020) [57] obtained wave impedance parameters based on SMI under the constraints of convolution models and identified thin layers in sandstone reservoirs.

To predict lithium brines in the L area of the Northeastern Sichuan Basin in China, we propose a workflow using seismic and logging data. In this workflow, seismic waveforms were clustered to establish a dataset for mapping the relationship between the waveforms and well-logging properties. Subsequently, the target properties were divided into high- and low-frequency components according to the best cutoff frequency of the well-logging data and predicted separately. Finally, the lithium brine reservoirs were predicted based on the anticipated results of the target properties, which were verified to match the geochemical test results of the validation wells.

2. Methodology

2.1. Porosity and Water Saturation Calculation

High porosity and water saturation are prerequisites for high-quality lithium brine reservoirs (with high total water content); therefore, it is necessary to estimate and predict the porosity and water saturation in the formation. Clavier et al. (1971) [58] improved the equation for calculating shale content (V_{sh}) using gamma-ray logs based on the sedimentation time of different rocks, as follows:

$$V_{sh} = \left[1.7 - (I_{GR} + 0.7)^2\right]^{\frac{1}{2}}, \tag{1}$$

and

$$I_{GR} = \frac{GR_{\log} - GR_{\min}}{GR_{\max} - GR_{\min}}, \tag{2}$$

where GR_{log} is the gamma-ray log reading, GR_{max} is the gamma-ray with 100% clay, and GR_{min} is the gamma-ray with 100% dolomite. The presence of pores has a significant impact on the elastic properties of rocks. Atlas (1995) [59] proposed that density logging is an effective way to measure porosity. The equation for calculating porosity based on the density logging curves is

$$\phi_T = \frac{\rho_m - \rho_b}{\rho_m - \rho_f}, \tag{3}$$

where ρ_m, ρ_b, and ρ_f are the densities of the matrix, fluid, and bulk fluids, respectively. However, because of the presence of mud in the rock and the inconsistency between the density of the mudstone and that of the matrix, it is necessary to correct Equation (3) for the mud content as follows:

$$\phi = \phi_T - V_{sh} \times \frac{\rho_m - \rho_{sh}}{\rho_m - \rho_f}, \tag{4}$$

where ρ_{sh} is clay density, which is generally obtained from a density-neutron crossplot. Water saturation is an important physical parameter that quantifies the water content in brine reservoirs. Water saturation (S_w) in carbonate reservoirs can be calculated using the following equation proposed by Archie (1941) [60]:

$$S_w = \left[\frac{aR_w}{\phi^m \times R_t}\right]^{\frac{1}{n}}, \tag{5}$$

where a, m, and n are the formation-factor coefficient, cementation exponent, and saturation exponent, respectively. R_w and R_t represent the formation water and deep resistivity, respectively.

2.2. Prediction of Well-Logging Properties Constrained by Waveform Clustering

Another characteristic of high-quality lithium brine is its low resistivity caused by its strong conductivity. Predicting electrical properties using seismic inversion methods is challenging because seismic data reflect the elastic characteristics of the medium rather than its electrical properties. To address this issue, we propose a novel workflow for high-quality lithium brines based on waveform clustering constraints. The lateral variation in seismic signals represents geological features, such as sedimentary facies and reservoir characteristics. This variation also reflects changes in the logging curves, such as natural gamma rays, resistivity, and acoustic impedance. Therefore, under the constraint of the lateral variation in seismic signals, information on the spatial location between wells can be obtained from the corresponding relationship between the logging data and seismic signals. This correspondence connects relatively high-frequency logging information with low-frequency seismic information. The waveform-constrained logging property prediction method includes the following steps: seismic waveform clustering analysis based on singular value decomposition (SVD), establishment of logging curve sample sets for different seismic faces, analysis of the cutoff frequencies, establishment of an initial model with the average value of logging attributes in the sample sets, and random prediction and iterative updates of logging attributes in different seismic faces and frequency ranges.

2.2.1. Waveform Clustering Based on SVD

SVD is a commonly used data-transformation method that aims to cluster data by transforming them into low-dimensional coordinate systems. The seismic signal matrix $\boldsymbol{S}$ consists of m seismic waveform samples, each with n sample points, forming an m $\times$ n matrix as follows:

$$\boldsymbol{S} = \begin{bmatrix} c_{11} & c_{12} & \cdots & c_{1n} \\ c_{21} & c_{22} & \cdots & c_{2n} \\ \vdots & \vdots & \ddots & \vdots \\ c_{m1} & c_{m2} & \cdots & c_{mn} \end{bmatrix}, \tag{6}$$

where c_{mn} denotes the n-th sampling point of the m-th seismic wavelet unit. Matrix $\boldsymbol{S}$ can be derived from the orthogonal matrices $\boldsymbol{U} \in \mathbf{R}^{m\times m}$ and $\boldsymbol{V} \in \mathbf{R}^{n\times n}$ as:

$$\begin{cases} \boldsymbol{S} = \boldsymbol{U\Lambda V}^{\mathrm{T}} \\ \boldsymbol{\Lambda} = \begin{bmatrix} \boldsymbol{\Lambda}_1 & 0 \\ 0 & 0 \end{bmatrix} \end{cases}, \tag{7}$$

where the column vectors of the orthogonal matrix $\boldsymbol{U} = [\boldsymbol{u}_1, \boldsymbol{u}_2, \ldots, \boldsymbol{u}_m]$ are the eigenvectors of $\boldsymbol{AA}^{\boldsymbol{T}}$ and orthonormal, respectively. The column vectors of the orthogonal matrix $\boldsymbol{V} = [\boldsymbol{v}_1, \boldsymbol{v}_2, \ldots, \boldsymbol{v}_n]$ are the eigenvectors of $\boldsymbol{A}^{\boldsymbol{T}}\boldsymbol{A}$ and are orthonormal to each other. $\boldsymbol{\Lambda}_1 = diag(\lambda_1, \lambda_2, \ldots, \lambda_p)$, where $\boldsymbol{\Lambda}_1$ is a diagonal matrix whose diagonal elements are the singular values of $\boldsymbol{A}$ sorted in descending order ($\lambda_1 \geq \lambda_2 \geq \ldots \geq \lambda_p$). Equation (6) can be expanded as follows:

$$\begin{aligned}
\boldsymbol{S} &= \boldsymbol{U\Lambda V}^{\mathrm{T}} \\
&= \begin{bmatrix} \boldsymbol{u}_1 & \boldsymbol{u}_2 & \cdots & \boldsymbol{u}_m \end{bmatrix} \begin{bmatrix} \boldsymbol{\Lambda}_1 \\ \boldsymbol{0} \end{bmatrix} \begin{bmatrix} \boldsymbol{v}_1 & \boldsymbol{v}_2 & \cdots & \boldsymbol{v}_n \end{bmatrix}^{\mathrm{T}} \\
&= \begin{bmatrix} \lambda_1\boldsymbol{u}_1 & \lambda_2\boldsymbol{u}_2 & \cdots & \lambda_n\boldsymbol{u}_n \end{bmatrix} \begin{bmatrix} \boldsymbol{v}_1{}^{\mathrm{T}} \\ \boldsymbol{v}_2{}^{\mathrm{T}} \\ \vdots \\ \boldsymbol{v}_n{}^{\mathrm{T}} \end{bmatrix} \\
&= \sum_{i=1}^{n} \lambda_i \boldsymbol{u}_i \boldsymbol{v}_i{}^{\mathrm{T}}
\end{aligned}, \tag{8}$$

Consider a seismic waveform $\boldsymbol{S_k}$ in matrix $\boldsymbol{S}$ as an example, which can be derived using Equation (8):

$$\boldsymbol{s}_k = \begin{bmatrix} \lambda_1 u_{1,k} & \lambda_2 u_{2,k} & \cdots & \lambda_n u_{n,k} \end{bmatrix} \cdot \begin{bmatrix} \boldsymbol{v}_1{}^{\mathrm{T}} & \boldsymbol{v}_2{}^{\mathrm{T}} & \cdots & \boldsymbol{v}_n{}^{\mathrm{T}} \end{bmatrix}^{\mathrm{T}}, \tag{9}$$

where $u_{n,k}$ represents the coordinate of vector $\boldsymbol{u_n}$ at point k.

The aforementioned matrix transformation process involves constructing a new orthogonal coordinate system with the direction vector $\boldsymbol{v}_1 \quad \boldsymbol{v}_2 \quad \cdots \quad \boldsymbol{v}_n$ as the coordinate axis. The singular value λ_i is the scaling factor from vector $\boldsymbol{u}_i$ to coordinate axis v_i. $\lambda_i u_{i,k}$ represents the coordinate value of the seismic waveform $\boldsymbol{s_k}$ on the coordinate axis v_i. Additionally, larger singular values correspond to larger scaling factors and larger variance and dispersion of coordinate values on the coordinate axis v_i. Therefore, larger singular values correspond to more important coordinate axes (Golub and Loan, 2013) [61].

Therefore, the part corresponding to the smaller singular values can be considered to represent a negligibly weak signal. According to Equations (8) and (9), only the dominant q $(q < p)$ singular values are retained, and the matrix $\boldsymbol{S}$ and seismic waveform $\boldsymbol{s_k}$ are simplified as:

$$\boldsymbol{S} \approx \sum_{i=1}^{q} \lambda_i \boldsymbol{u}_i \boldsymbol{v}_i{}^{\mathrm{T}} = \begin{bmatrix} \lambda_1\boldsymbol{u}_1 & \lambda_2\boldsymbol{u}_2 & \cdots & \lambda_q\boldsymbol{u}_q \end{bmatrix} \cdot \begin{bmatrix} \boldsymbol{v}_1{}^{\mathrm{T}} & \boldsymbol{v}_2{}^{\mathrm{T}} & \cdots & \boldsymbol{v}_q{}^{\mathrm{T}} \end{bmatrix}^{\mathrm{T}}, \tag{10}$$

and

$$\boldsymbol{s}_k = \begin{bmatrix} \lambda_1 u_{1,k} & \lambda_2 u_{2,k} & \cdots & \lambda_q u_{q,k} \end{bmatrix} \cdot \begin{bmatrix} \boldsymbol{v}_1{}^{\mathrm{T}} & \boldsymbol{v}_2{}^{\mathrm{T}} & \cdots & \boldsymbol{v}_q{}^{\mathrm{T}} \end{bmatrix}^{\mathrm{T}}. \tag{11}$$

From Equations (10) and (11), the coordinate system $\boldsymbol{v}_1 \quad \boldsymbol{v}_2 \quad \cdots \quad \boldsymbol{v}_n$ is simplified into a low-dimensional coordinate system $\boldsymbol{v}_1 \quad \boldsymbol{v}_2 \quad \cdots \quad \boldsymbol{v}_q$ after ignoring the directions with smaller data variances. After simplification, the coordinate values $\lambda_i u_{i,k}$ of the seismic waveform $\boldsymbol{s}_k$ in the low-dimensional coordinate system can be used to reflect the characteristics of the seismic waveform. In a low-dimensional coordinate system, the seismic waveforms that are closer in coordinates are more similar. The coordinates of the seismic waveform $\boldsymbol{s}_k$ on the first q-coordinate axes can be used as indicators for dimensionality reduction and can be set as follows:

$$\boldsymbol{Y}_k = \begin{bmatrix} y_{k,1} & y_{k,2} & \cdots & y_{k,q} \end{bmatrix} = \begin{bmatrix} \lambda_1 u_{1,k} & \lambda_2 u_{2,k} & \cdots & \lambda_q u_{q,k} \end{bmatrix}. \tag{12}$$

Subsequently, the number of samples used to construct each seismic waveform is reduced from n to q. $\boldsymbol{Y_k}$, as the kth element, constitutes the set of m seismic waveforms:

$$\boldsymbol{Y} = \begin{bmatrix} \boldsymbol{Y}_1 & \boldsymbol{Y}_1 & \cdots & \boldsymbol{Y}_m \end{bmatrix} \tag{13}$$

The singular values corresponding to each coordinate axis represent the importance of that direction; therefore, they should be used as weights for dimensionality reduction. After normalizing the singular values to sum them to 1, a weight vector can be constructed as:

$$\boldsymbol{W} = \begin{bmatrix} w_1 & w_1 & \cdots & w_q \end{bmatrix}. \tag{14}$$

Subsequently, the clustering of the dimensionality-reduced data was based on the K-means algorithm (Hartigan and Wong, 1979) [62]. The weighted Euclidean distance was used as the similarity criterion. Assuming the presence of r clusters, r samples were randomly selected from set $\boldsymbol{Y}$ as the initial cluster centers. All samples were divided into the nearest cluster centers based on their weighted Euclidean distances. The weighted distance from sample $\boldsymbol{Y_k}$ to the t-th cluster center $\boldsymbol{m}_t = \begin{bmatrix} m_{t,1} & m_{t,2} & \cdots & m_{t,q} \end{bmatrix}$ was derived as:

$$d(k,t) = \sqrt{w_1 \left| y_{k,1} - m_{t,1} \right|^2 + \cdots + w_q \left| y_{k,q} - m_{t,q} \right|^2}. \tag{15}$$

The mean value of each cluster of samples was used as the new cluster center. The termination condition for the iterative update was whether the cluster center converged. This process performs the clustering analysis of seismic waveforms.

2.2.2. Sample Set of Well-Logging Properties and Frequency Analysis

After completing the waveform clustering analysis and well seismic calibration, well-logging properties (such as resistivity and density) in the well were also clustered based on their corresponding seismic waves. Subsequently, the mapping relationship between the seismic waves and well-logging properties was established. Although seismic waves in the same waveform cluster may correspond to some well-logging property segments, the logging properties in this cluster had certain differences. To distinguish the differences in well-logging properties in a seismic waveform cluster, the properties of the target position were not predicted by selecting all well-logging properties in the cluster; however, the c wells (the number of effective samples) that have the closest seismic waveform as the sample set of that position were selected.

The well-logging properties in the sample set did not match completely; however, they did match in certain frequency ranges. Therefore, it was necessary to perform a matching analysis of well-logging properties in the sample set. The wavelet transform can simultaneously characterize the signals in both the time and frequency domains and quantitatively predict the low-frequency stable part and high-frequency abrupt change part of the signals; therefore, it is suitable for the matching analysis of well-logging data. To obtain the best cutoff frequency of the well-logging curves in the sample set, the wavelet transform algorithm was used to calculate the difference between the well-logging property L and average value $\overline{L}$ in different frequency ranges $(0, f)$:

$$O(f) = \arg(\min \left\| L - \overline{L} \right\|) = \arg(\min \left\| \int_0^f \varphi(\omega, t) - \overline{L} \right\|), \tag{16}$$

where $\varphi(\omega, t)$ is the wavelet transform function, and ω and t are the frequency and time, respectively, as the parameters of wavelet transform.

2.2.3. Prediction in Different Frequency Ranges under Seismic Waveform Constraints

Based on the best cutoff frequency, the logging properties of the target location were divided into low- and high-frequency parts (the high and low frequencies of this band were relative to the logging data, and this frequency was generally higher than the seismic frequency band). Under the constraint of waveform clustering, the low-frequency part uses a Markov Chain Monte Carlo random simulation algorithm (Zhu and Gibson, 2018; de Figueiredo et al., 2019) [63,64].

Firstly, a Markov Chain, denoted as X_n, was constructed. It comprised random variables, and it was used for sampling and satisfied conditional probability distribution function:

$$P(X_{n+1} = x|X_0, X_1, \ldots, X_{n-1}) = P(X_{n+1} = x|X_n). \quad (17)$$

It should also satisfy the property that different states converge to a stationary distribution after successive iterations over time. When the Markov Chain reaches a stationary distribution, the sampled points ($h(X^i)$) are used to estimate the expectation of a target parameter's function with Monte Carlo integration:

$$E = \frac{1}{n-m}\sum_{i=m+1}^{n} h(X^i), (0 < m < n). \quad (18)$$

Subsequently, an appropriate distribution of random sample points was obtained based on the conditional probability distribution function of reservoir parameters. By iteratively perturbing model parameters and performing multiple random simulations of initial model parameters, reservoir parameters were simulated using the stochastic sampling algorithm.

The high-frequency part also used a random simulation algorithm; however, it did not require the constraint of seismic faces but required that of the prior probability distribution in the sample set. The common part, which is the average value of the sample set, was used as the initial model for performing the iterative calculations to obtain high-resolution simulation results. Therefore, the results of the high-frequency part were simulated based on existing probability distributions. The reliability of the high-frequency part was lower than that of the low-frequency part. Additionally, during the property prediction process, a stratigraphic smoothing constraint was used based on a certain smoothing radius. The predicted results for the target points must satisfy the average value within the smoothing radius.

2.3. Workflow

In summary, the prediction of a lithium brine reservoir based on seismic data and well log data included the following steps: First, the sensitive logging properties of the reservoir were determined based on known well information as the target property to be predicted. Subsequently, clustering analysis of the seismic waveforms was performed using the SVD algorithm. Logging property sample sets were established for the target locations based on their waveform clusters. Based on the cutoff frequency, the logging properties were divided into low- and high-frequency parts, which were then separately predicted with random simulations. The workflow is illustrated in Figure 1.

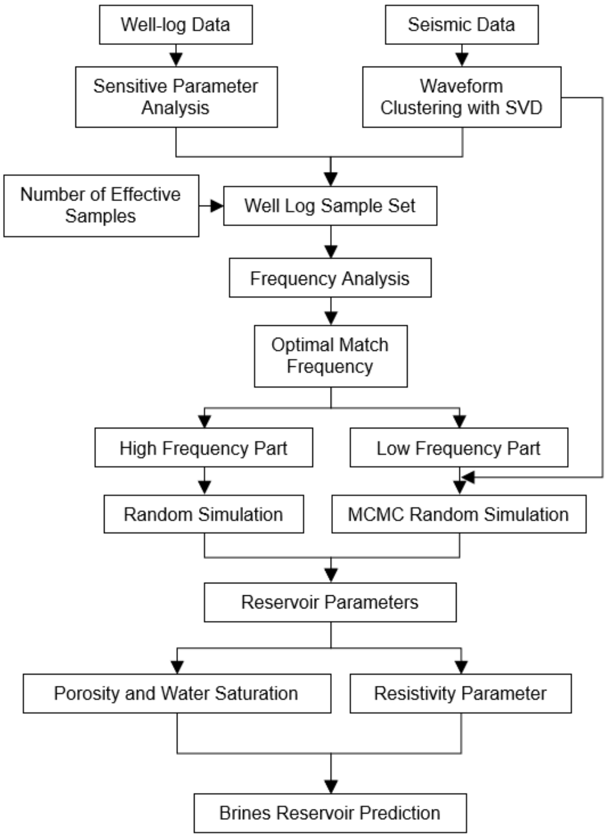

Figure 1. Flowchart of the lithium brine reservoir prediction process constrained by waveform clustering.

3. Geologic Setting and Data Description

Sichuan Foreland Basin is a basin in western China, located on the western margin of the Yangtze Plate, bordered to the north by the Qinling orogenic belt, the southeast by the Qiye Mountains, and the west by the Songpan–Ganzi orogenic belt. The basin took shape during the Indosinian period, and the Late Triassic Indosinian movement formed an inland lake basin. The current structural topography was formed after the intense folding and faulting effects of the Himalayan movement. Area L (the blue quadrilateral in Figure 2) is located in the northeastern Sichuan Basin, a steep structural belt in the eastern Sichuan Basin (Gu et al., 2019) [65] The stratigraphic column of the Triassic strata in this area is shown in Figure 3. This study examined Lower and Middle Triassic strata (consisting of the Feixianguan, Jialingjiang, and Leikoupo Formations from bottom to top), which comprise marine carbonate deposits formed during the late Indosinian tectonism with a thickness of approximately 900–1700 m. The maximum exploration depth in this study area is 6000 m. This area belongs to a continental shelf-type carbonate platform mainly formed by evaporation and includes facies, such as grain beaches and restricted lagoons, with uneven lateral variation. The main lithology is dolomite, followed by limestone, with interbedded gypsum salt distributed between the dolomite and limestone. Some strata in the target layers contain tuffaceous rock, indicating that the formation belonged to a salt-lake sedimentary environment at that time. The gypsum salt layers within the Triassic strata provide a material basis for enriching lithium brines.

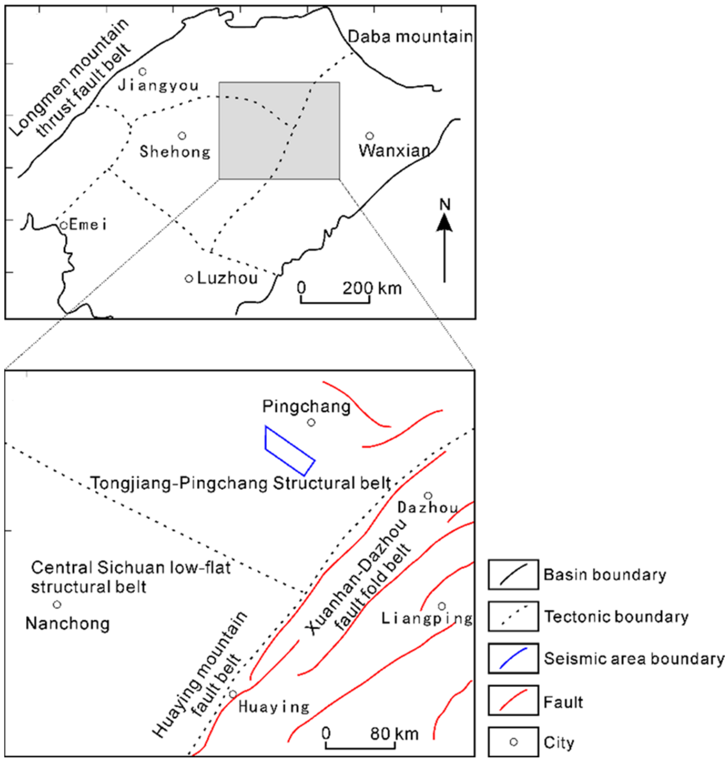

Figure 2. The tectonic framework of the Sichuan Basin. The study area is highlighted with a blue quadrilateral (Zhang et al., 2022) [21].

During the sedimentation process, the climate is arid, and seawater gradually evaporates and concentrates. The area of marine evaporite gradually increases, causing various elements to converge toward the center of the basin and accumulate rich mineral deposits (Zhang et al., 2022) [21]. The strong evaporation of seawater and dry air leads to a continuous concentration of seawater, and the concentration of internal elements gradually increases (Huang, 2013) [66]. The hot and arid ancient climate also accelerates the chemical reaction process of substances, leading to the rapid precipitation of minerals containing multiple ions.

As a typical carbonate reservoir, the target reservoir exhibits large lithological differences, a complex pore–permeability relationship, and irregular changes in the physical property. The complex lithological variations in this area pose challenges to the resolution of seismic data. A total of 1200 km^2 of three-dimensional (3D) seismic data are available for area L (Figure 4). Twenty-two wells are located within the seismic data region. The three seismic sections (sections 1–3 in Figure 4) are shown in Figure 5. The amplitude spectrum of the seismic data within the target layer had a dominant frequency of 40 Hz (Figure 6). The lateral variation in the seismic waveform was unstable. The known chemical properties of the brine in the eight wells (Table 1) show that the brines from three wells (L11, L172, L3) contain relatively high amounts of lithium. The well log curves and interpretation data for well L11 are displayed in Figure 7. The Li-rich brine reservoir is in the layers of the Feixianguan Formation. The dominant porosity range of the dolomite reservoir in this target layer was 2%–8%, with a range of water saturation of 10–100 (Figure 7).

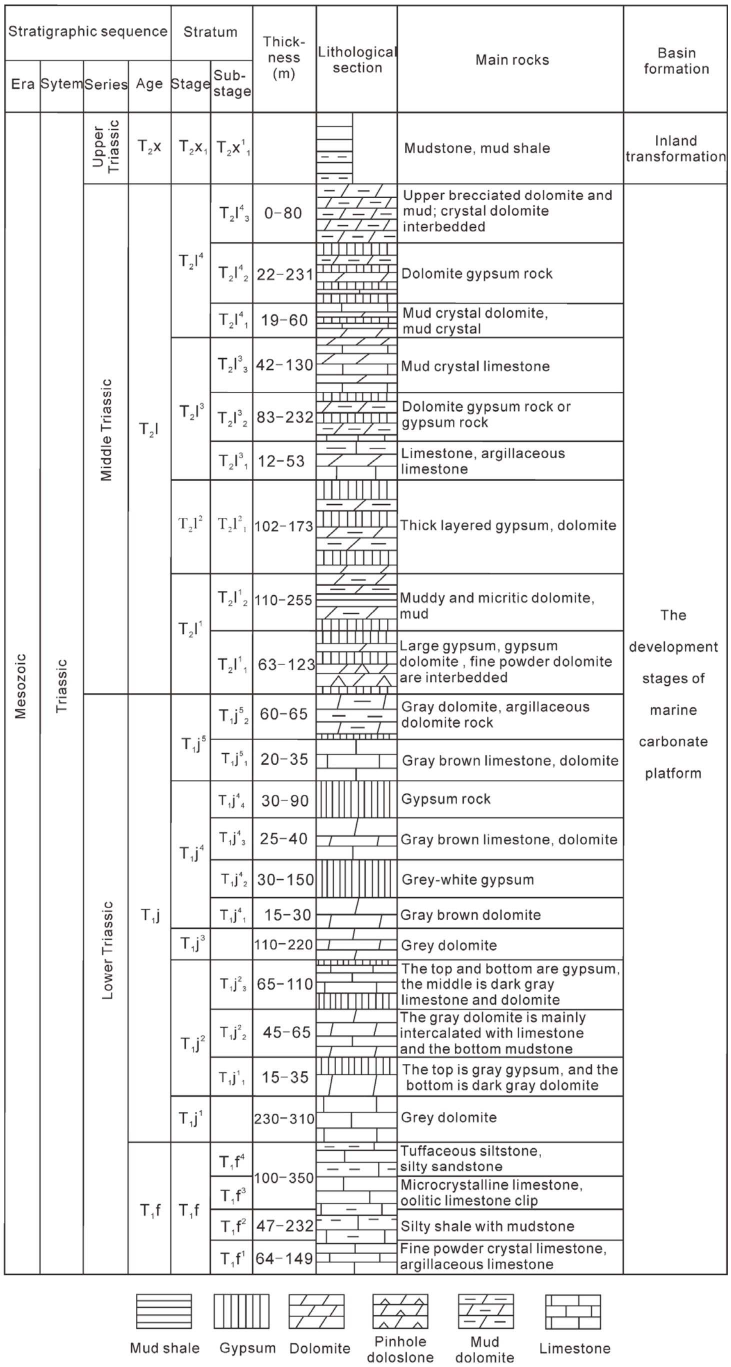

Figure 3. Stratigraphic description of the target layers in the L area.

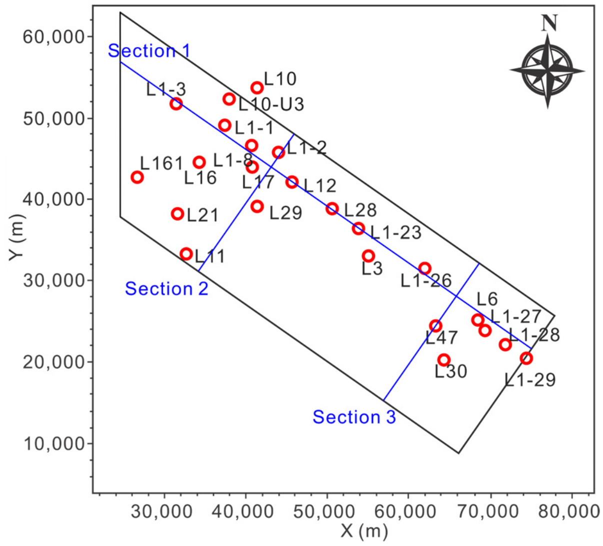

Figure 4. Three-dimensional seismic data region and well locations. Section 1 is in line with the most wells. Sections 2 and 3 are two xlines located in the high part of the structure.

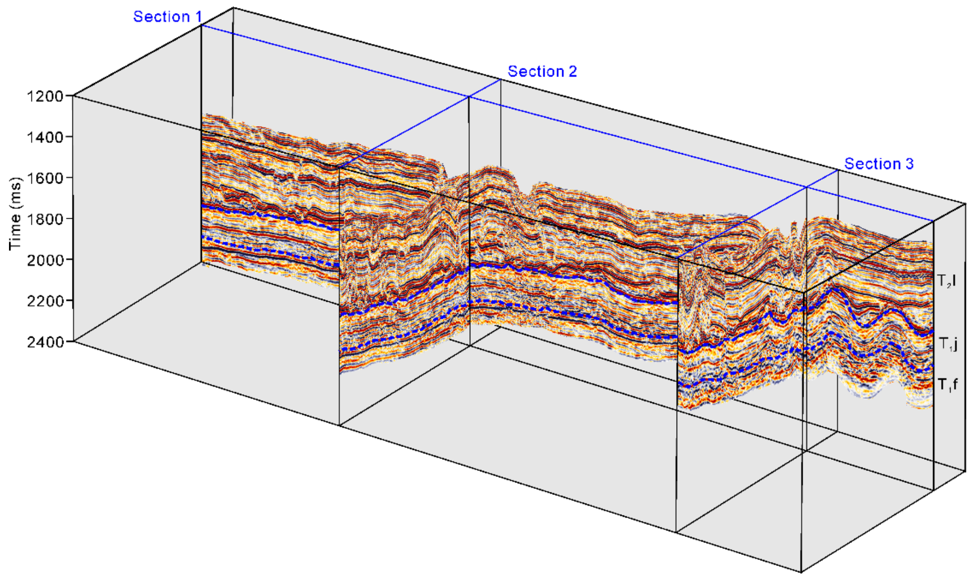

Figure 5. Seismic sections within the study area. The blue dashed lines denote the interfaces between Feixianguan (T_1f), Jialingjiang (T_1j), and Leikoupo (T_2l) Formations.

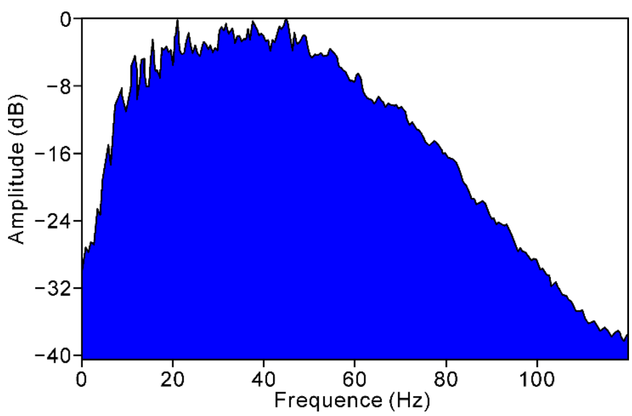

Figure 6. Seismic amplitude spectrum of the target layers.

Table 1. Elemental content of the brine in various wells.

Well Name	Stratum	Li^+ (mg/L)	Br^- (mg/L)
L11	T1f	32.95	150
L172	T2l4	25.9	116
L3	T1f3-T1f1	25.1	225
L177	T2l4	17.7	105
L16	T2l4	13.18	709
L21	T1f3	10.4	173
L170	T1j4	7.565	156
L17	T2l4	7.79	/

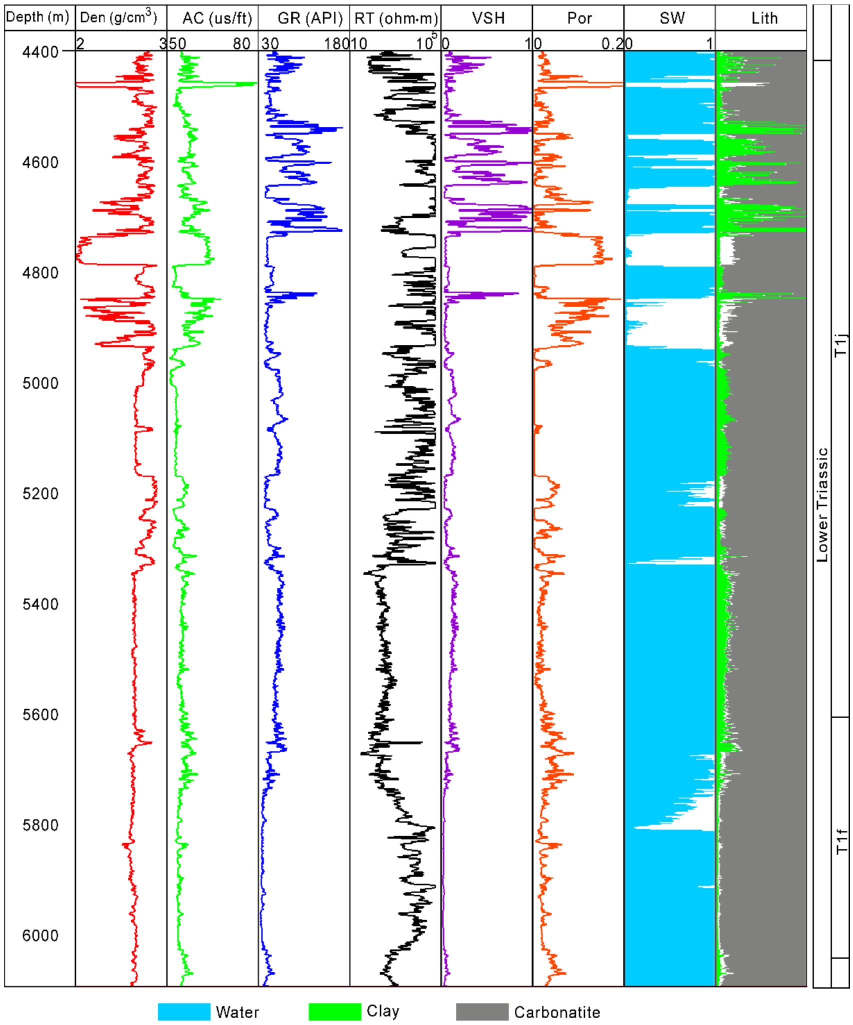

Figure 7. Logging data and interpretation results for well L11. These log curves are the sonic differential time of P-wave (AC), natural gamma (GR), resistivity (RT), the volume of shale (VSH), porosity (Por), water saturation (SW), and lithology (Lith) from left to right.

4. Application

The proposed workflow was applied to real 3D seismic data for lithium brine reservoir prediction in the Lower and Middle Triassic strata in the L area.

4.1. Sensitive Parameter Analysis

The lithium brine layer was identified based on the elemental content of the brine produced in the production well. To analyze the sensitivity parameters of the target reservoir, a cross-plot was compiled using well-logging data from the known brine layer wells in the study area (Figure 8). Most Li-rich and other formations have the same acoustic time difference and natural gamma, and their distribution range has no clear boundary. Therefore, the natural gamma and acoustic travel times are insensitive to the brine layers. In contrast, the distribution range of resistivity between the Li-rich and other formations in Figure 8 has a relatively clear boundary (near 200 ohm·m). Resistivity is a sensitive parameter for distinguishing the brine layers because of the presence of lithium ions in the brine, which enhances the conductivity of the reservoir and results in lower resistivity.

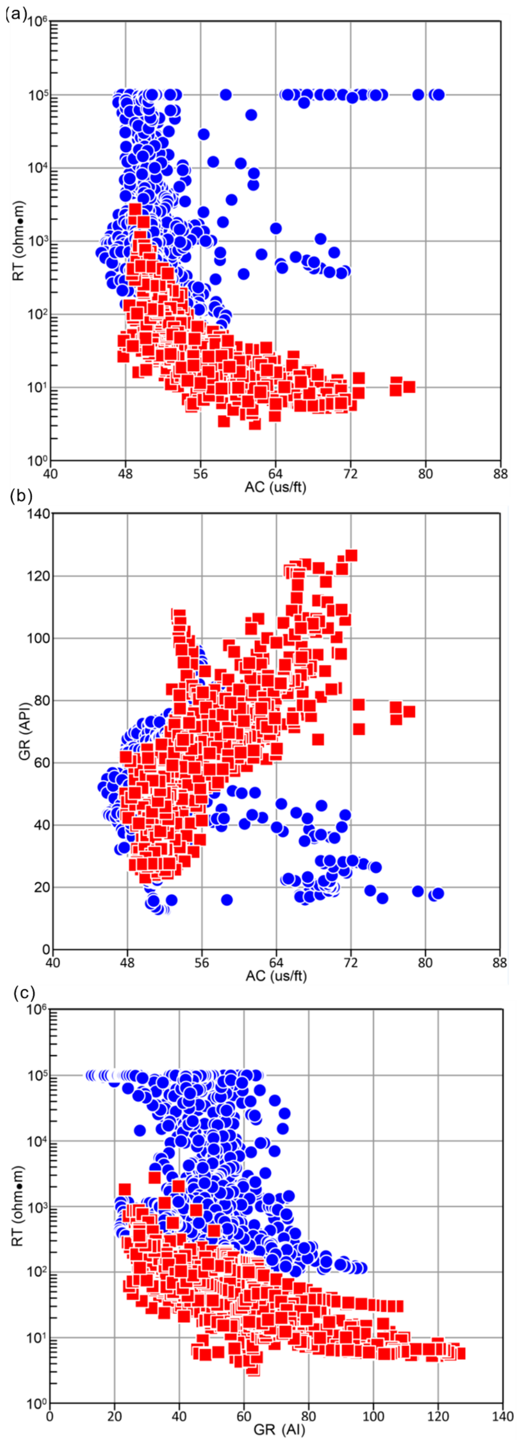

Figure 8. Cross-plot of logging data for the Li-rich (red points) and other formations (blue points). Where (**a**) AC, (**b**) RT, and (**c**) GR denote the sonic differential time of P-wave, resistivity, and natural gamma, respectively.

The relationship between brine layers and lithology is influenced by the genesis of the brine layers. Studies have indicated that brine deposits in the Sichuan Basin are widely developed within the Middle–Lower Triassic shallow marine carbonate series and the carbonate–evaporite series formations (Li et al., 2018) [67]. In the present area, the dominant lithologies include dolomite and gypsum rocks. Considering geological genesis analysis, the study area possesses favorable lithological conditions. Consequently, this predictive workflow does not further differentiate lithologies but directly uses the physical parameters in subsequent steps to predict areas of the lithium brine.

4.2. Number of Effective Samples Analysis

Firstly, we used a waveform classification approach based on SVD to classify the seismic signals within the target layer of the study area. Five classifications were conducted, and the classification results are illustrated in Figure 9. The results indicate that Wells L1-3, L161, and L1-2 belong to the same waveform category (waveform 4 in this figure). Multiple known wells belong to the same seismic cluster and serve as optional samples for that cluster. The computational efficiency of the prediction process is reduced when the number of samples is extremely large. When it is too small, it will reduce the accuracy of the calculation results. To determine the optimal number of effective samples, we analyzed the correlation between the logging properties of a certain well in the sample set and the known logging properties for different effective sample numbers. The correlation coefficients between the known resistivity properties of the well locations and those of the effective sample wells were calculated. The results for the four wells are shown in Figure 10. The correlation coefficients increased with an increase in the number of samples. In this study, six samples were selected between the top and bottom horizons as when the sample point is higher than six, the coefficient's increase is not significant. Under these conditions, the correlation coefficients of the four wells ranged from 0.54 to 0.64.

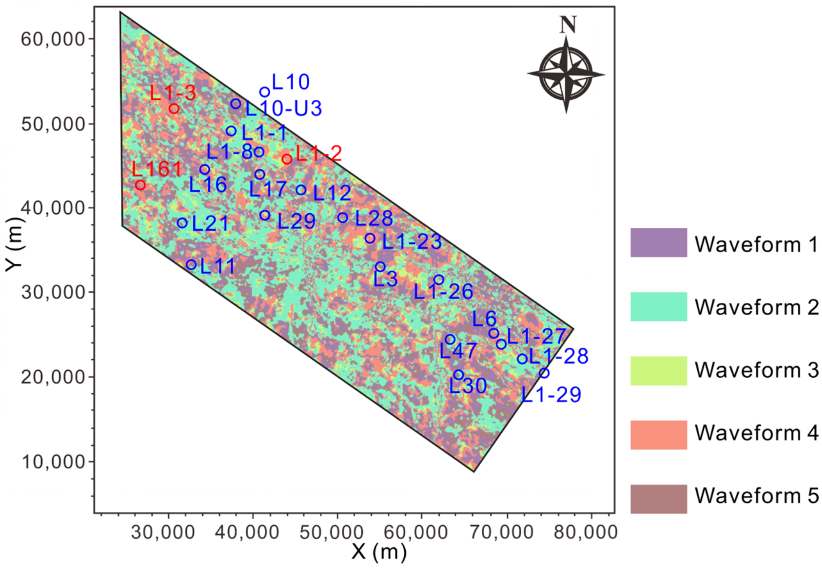

Figure 9. Waveform clustering results based on SVD. The five colors denote the five classifications.

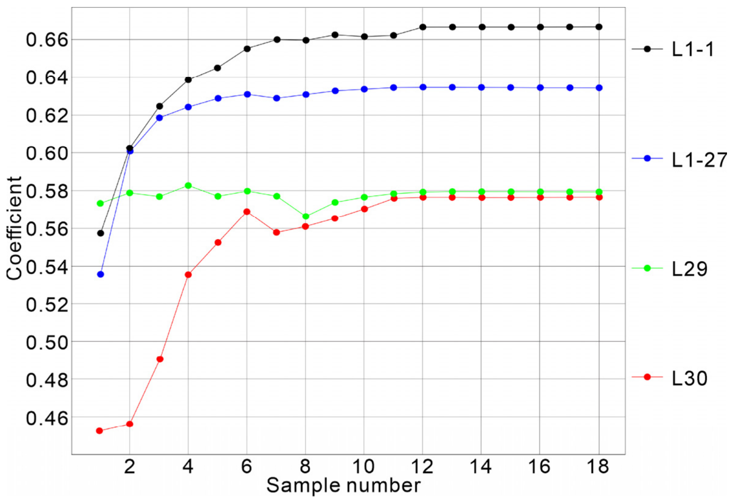

Figure 10. Analytical results for the effective sample number.

4.3. Best Cutoff Frequency Analysis

To analyze the optimal cutoff frequency, we selected two wells belonging to the same seismic waveform cluster. The seismic sections of the two wells are shown in Figure 11a. A comparison of the seismic traces near the two wells after layer matching exhibited a correlation coefficient of 0.93 (Figure 11b), indicating that the seismic waveforms of these two wells have similar characteristics. The original resistivity curves of the two wells had correlation coefficients of 0.686 (Figure 12a).

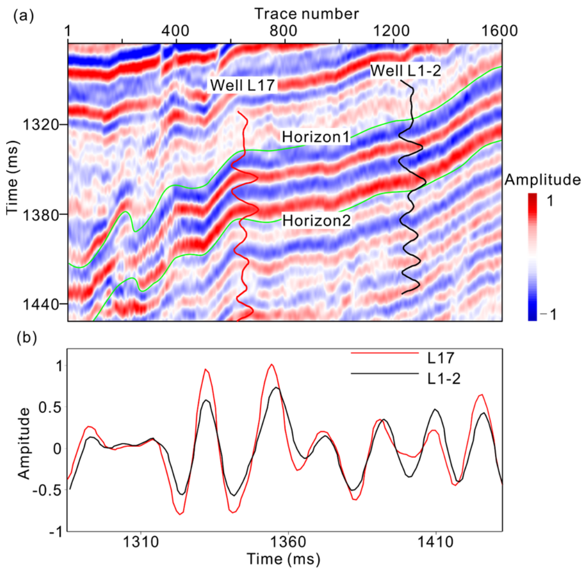

Figure 11. The seismic section (**a**) and seismic waveforms (**b**) of wells L17 and L1-2. Well L17 is matched along the horizon to the time domain of well L1-2.

We performed wavelet transform filtering on the well log curves (we converted well log curves to time domain based on time–depth relationships), retaining frequency ranges of 0–500, 0–300, 0–200, 0–150, and 0–100 Hz (Figure 12b–f), resulting in correlation coefficients of 0.720, 0.745, 0.879, 0.927, and 0.945, respectively. As the cutoff frequency decreased, the correlation coefficients of the resistivity curves of the two wells increased. In the frequency range of 0–100 Hz (Figure 12f), the correlation coefficient was comparable to that of the seismic waveforms. This result indicates that when the seismic waveforms corresponding to well-logging properties are similar, they can also exhibit a relatively high degree of similarity within a certain frequency band. This similarity was higher in the low-frequency range and lower in the high-frequency range. The high-frequency part of the well log properties was not influenced by the seismic waveforms. Therefore, predicting the target well log properties in different frequency bands is necessary.

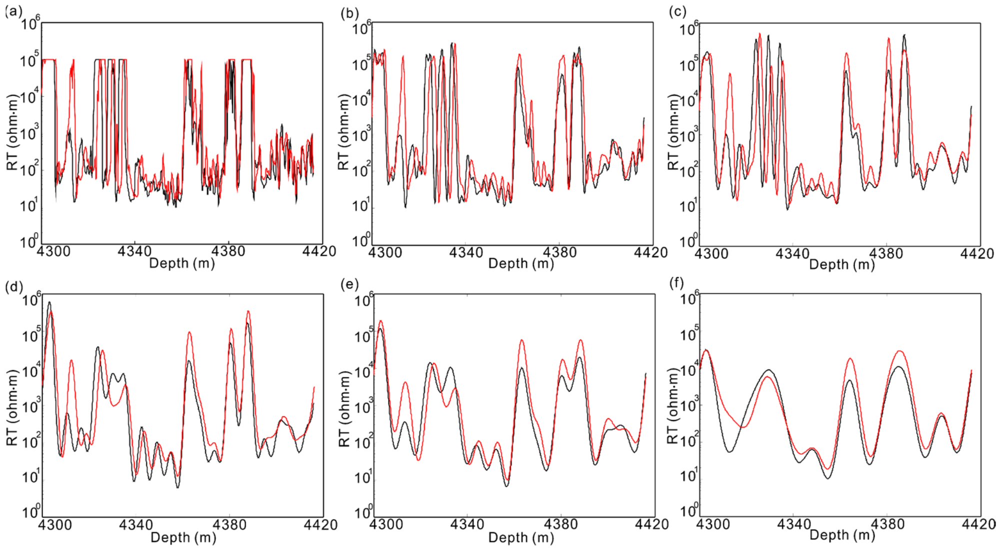

Figure 12. Resistivity curves for wells L17 (red curves) and L1-2 (black curves) at different frequency bands: (**a**) original curves, (**b**) 0–500 Hz, (**c**) 0–300 Hz, (**d**) 0–200 Hz, (**e**) 0–150 Hz, and (**f**) 0–100 Hz. RT denotes the resistivity.

To determine the optimal cutoff frequency, we calculated the correlation coefficients of well logs from all wells in the study area. The correlation coefficient represents the correlation between the resistivity data in the different frequency bands and the average resistivity log of the effective samples. The results from the four wells are shown in Figure 13; the correlation coefficients decreased with increasing frequency. The optimal cutoff frequency divides the target property into two parts for prediction. If the cutoff frequency is too low, the low-frequency part is consistent with the seismic data band, resulting in a high correlation coefficient. However, the resolution is limited within the seismic band. If the cutoff frequency is too high, the correlation coefficient is low, and the reliability of the low-frequency part decreases. Therefore, an appropriate cutoff frequency must be selected. In this study area, we selected a cutoff frequency of 120 Hz, which exceeded the seismic frequency band and had a high correlation coefficient.

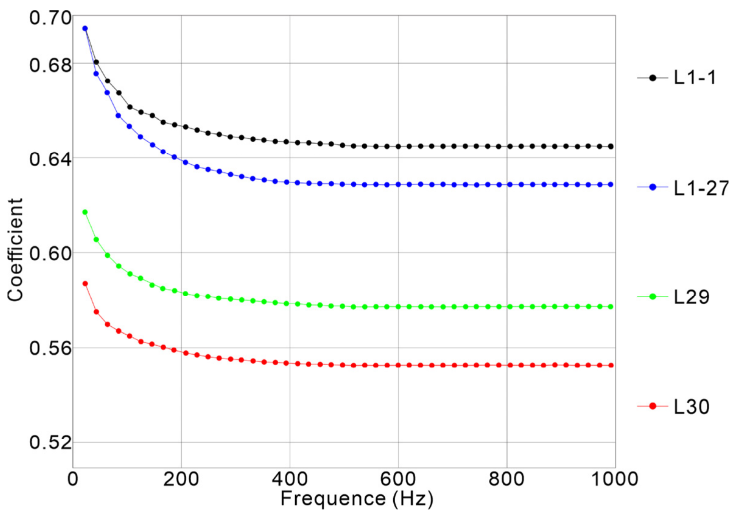

Figure 13. Analysis results of the optimal cutoff frequency.

4.4. Prediction and Verification Results

To compare the inversion results between the inversion method constrained by waveform clustering and the conventional model-based inversion method, we present the wave impedance inversion results of both approaches, as shown in Figure 14. The comparative analysis of the outcomes from these two methods reveals that the inversion method constrained by waveform clustering exhibits significantly higher resolution than the conventional model-based inversion method.

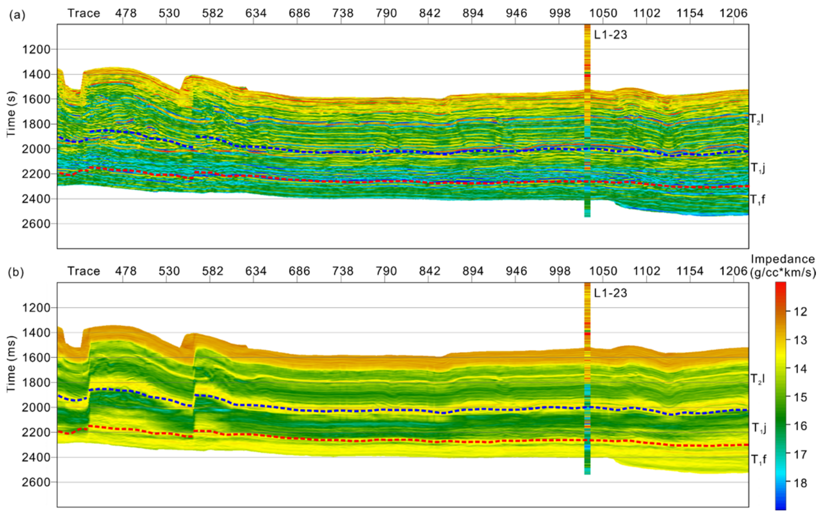

Figure 14. Impedance inversion results of (**a**) the inversion method constrained by waveform clustering and (**b**) the conventional model-based inversion method. The blue and red dashed lines denote the interfaces between the Feixianguan, Jialingjiang, and Leikoupo Formations.

Using a waveform cluster-controlled well-log property prediction method based on 3D seismic and well log data, we predicted the porosity, water saturation, and resistivity properties of the study area. The results are presented in Figure 15. The prediction results of the well-log properties showed high resolution, displaying distinct thin layers in the vertical direction and variations in biogenic reefs and flats in the horizontal direction. The results include the geological strata of the Feixianguan, Jialingjiang, and Leikoupo Formations. The results in Figure 15a indicate that the top layers of both the Jialingjiang and Leikoupo Formation are characterized by relatively high porosity, with uneven and discontinuous lateral variation. The results in Figure 15b indicate that the bottom layers of the Jialingjiang Formation had higher water saturation. The resistivity results in Figure 15c show that the Feixianguan and Leikoupo Formations had lower resistivity features. Combining the results of porosity, water saturation, and resistivity properties, the Feixianguan Formation in the middle of the study area was determined to be a high-quality reservoir. The prediction results of the resistivity based on the neural network method (Fu, 1997) [68] are shown in Figure 16.

To analyze the accuracy of the predicted well-log properties, the predicted results near the L1-23 well were compared with the information obtained from the well log (Figure 17). The comparison results in Figure 17a–c show better consistency than Figure 17d. Furthermore, we quantitatively compared the differences between the predicted results and actual values, as shown in Figures 18 and 19. Near the depth of 3900 m, there were relatively larger errors in both water saturation and porosity than at other depths. Although the predicted resistivity values using the proposed workflow had mostly large errors, the variation trends matched well with the true values. In contrast, the resistivity predictions based on the neural network had larger errors; however, the variation trends did not match with the true values.

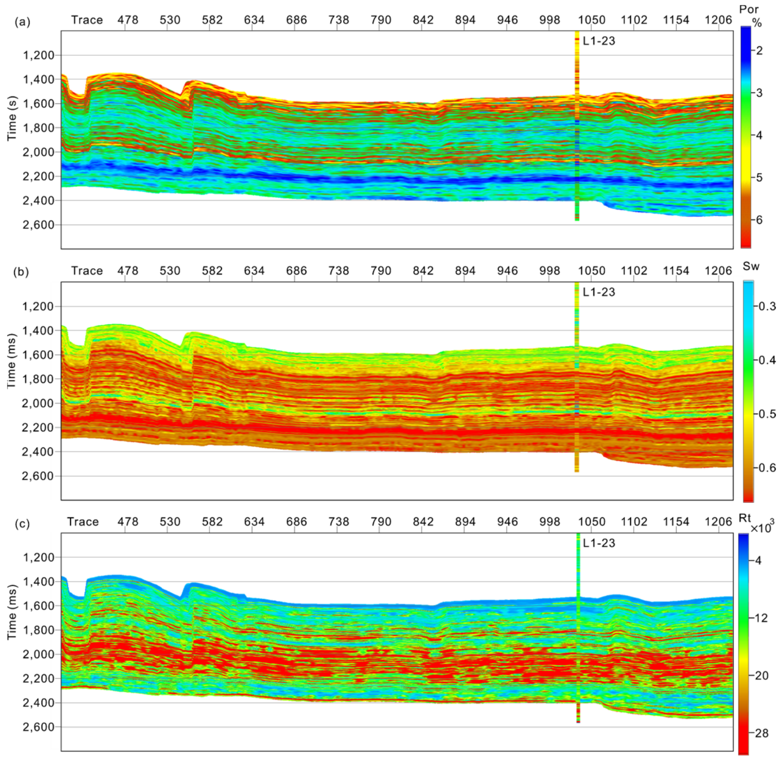

Figure 15. Prediction results of (**a**) porosity, (**b**) water saturation, and (**c**) resistivity. The blue and red dashed lines denote the interfaces between the Feixianguan, Jialingjiang, and Leikoupo Formations.

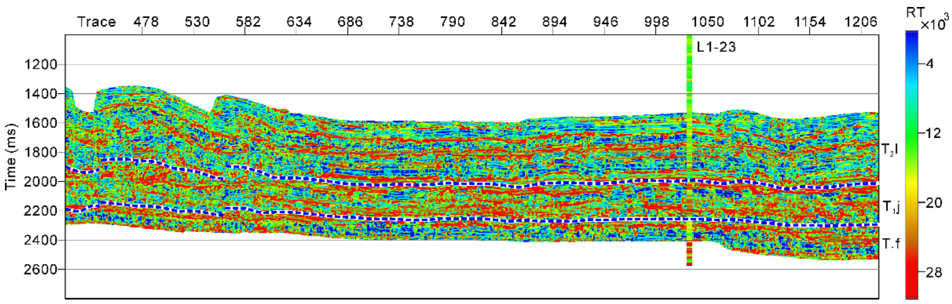

Figure 16. Results of the neural network-based resistivity prediction. The blue dashed lines denote the interfaces between the Feixianguan, Jialingjiang, and Leikoupo Formations.

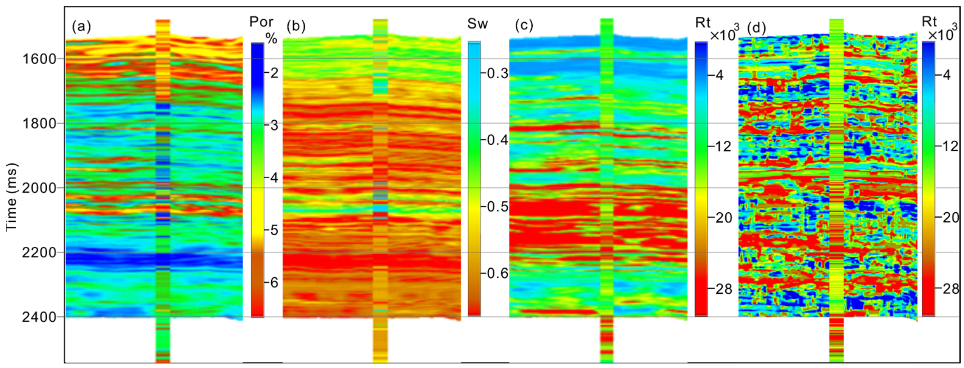

Figure 17. Local prediction results of porosity, water saturation, and resistivity near well L1-23. (**a**–**c**) are the results of the porosity, water saturation, and resistivity from the proposed workflow, respectively, and (**d**) is the results of the resistivity from the neural network-based method.

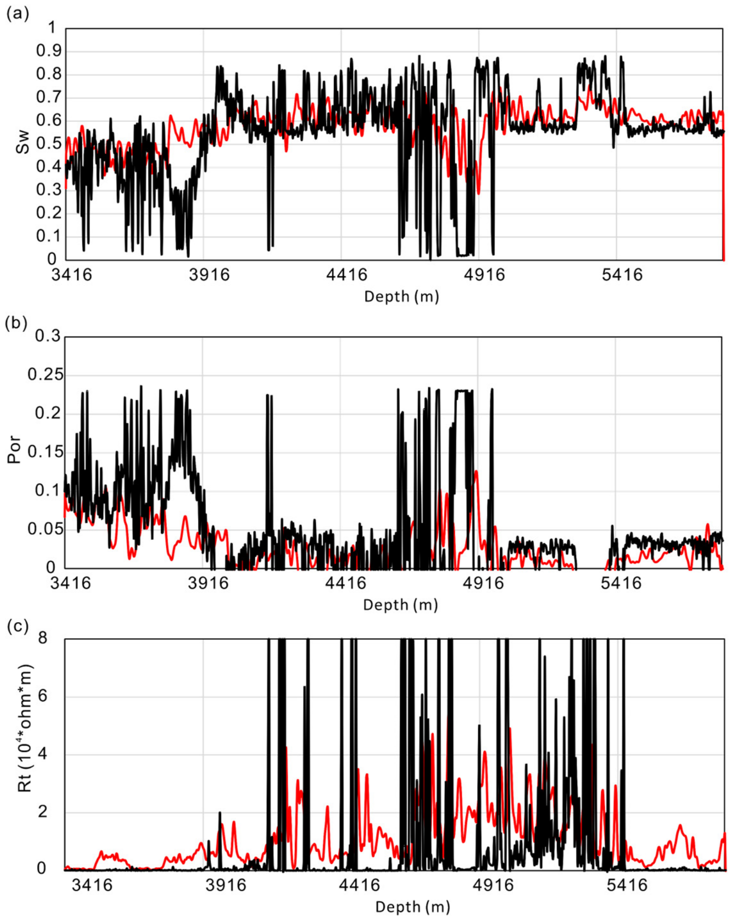

Figure 18. Comparison between predicted results (the red curves) and true logging data (the black curves) of well L1-23 from the proposed workflow (cf. Figure 1). (**a**–**c**) are the porosity, water saturation, and resistivity, respectively.

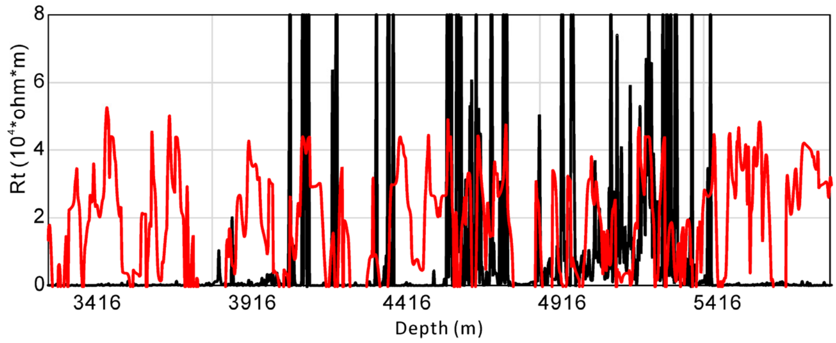

Figure 19. Comparison between predicted resistivity results (the red curve) and true logging data (the black curve) of well L1-23 from the neural network-based method.

We generated horizon slices of the Feixianguan Formation, as shown in Figure 20 (Figure 20a–c are the water saturation, porosity, and resistivity results, respectively). Wells L11 and L3 exhibit relatively high water saturation, porosity, and low resistivity, which belong to high-quality reservoirs. Well L16 shows high water saturation and low resistivity but lower porosity. Although well L21 has high water saturation, its porosity is relatively low, and resistivity is high. Well L17 shows relatively high water saturation and porosity but high resistivity. These three wells do not belong to high-quality reservoirs, which is consistent with the variation in lithium content shown in Table 1.

5. Discussion

The initial model of the waveform cluster-controlled well-log property prediction method was established using well log data acquired in the field. This model connects well log curves or log interpretation results to seismic waveform data. Therefore, it has a higher resolution than the seismic waveform data. The results within the optimal cutoff frequency based on the matching analysis of the well-log properties are highly reliable. However, outcomes that exceed the cutoff frequency range are acquired with random prediction, and their dependability is limited even when governed by the probability distribution.

During the process of establishing the well log property sample set, the geological horizons of different wells could not be completely matched in the depth domain, which led to the stretching and compression of different well log properties. Therefore, the control of geological horizons is necessary during this process. The more detailed the geological horizon interpretation, the more accurate the matching between different well log properties. Therefore, an accurate and adequate interpretation of geological horizons is a prerequisite for this method. The number of effective samples and optimal cutoff frequency are two important parameters in the workflow. The values of these parameters must be adjusted based on the actual situation. In practical applications, both the efficiency and accuracy of the method must be considered. Further research is needed to quantify how these parameters affect the workflow results.

The workflow predicts high-quality reservoirs based on the electrical characteristics, water saturation, and porosity of the lithium brine reservoirs. However, in oilfield brines, other elements, such as potassium, often coexist with lithium, enhancing conductivity and lowering resistivity, thereby leading to ambiguity in interpretation. This implies that locations with low electrical resistivity and high water saturation may contain other elements leading to low water resistivity within the reservoir. The presence of lithium elements in the reservoir near a specific well can only be confirmed when the lithium content of that well is known. Therefore, this method is reliable near wells with known lithium content, and the results are constrained by the hydrochemical test data. However, the reliability of predicting lithium brine reservoirs in other wells was low. Currently, it is difficult to distinguish between different elements in oilfield brines with different geological origins using seismic data only. Therefore, in future studies, we plan to integrate this workflow with geological genesis methods to predict the distribution of brine reservoirs containing different elements.

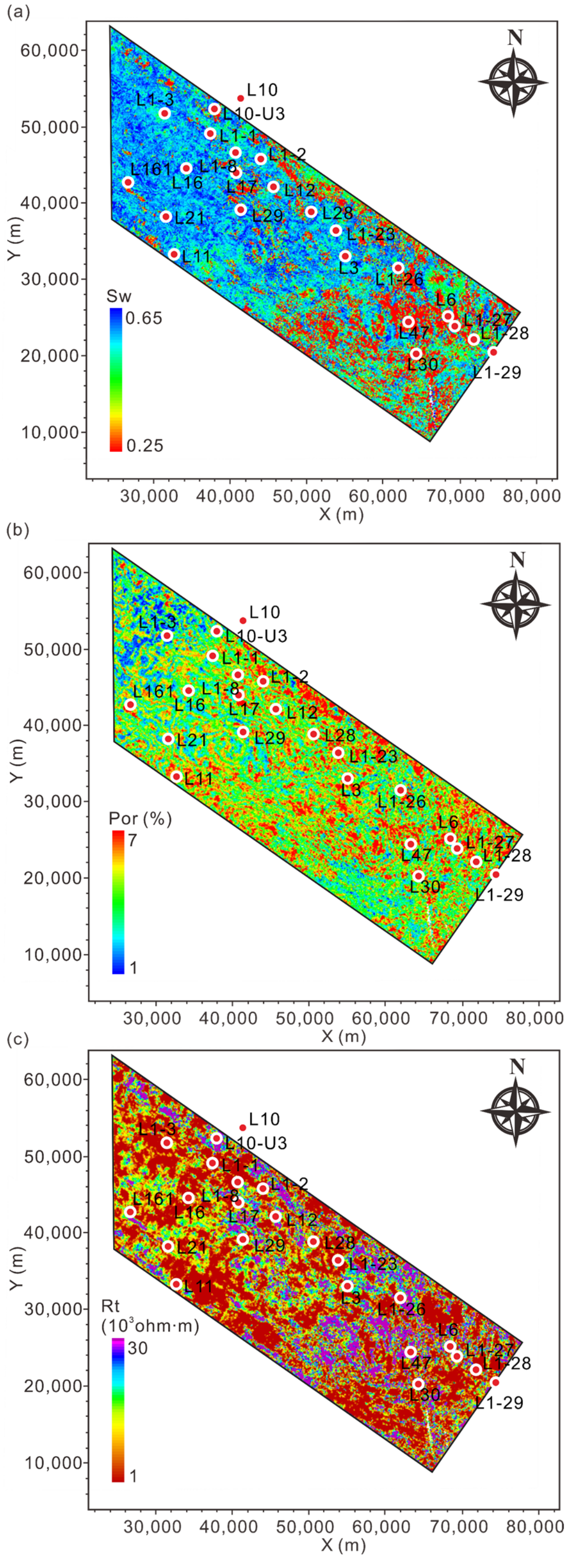

Figure 20. Horizon slices of water saturation (**a**), porosity (**b**), and resistivity (**c**) results from the Feixianguan Formation.

6. Conclusions

Variations in seismic waveforms are caused by changes in geological and reservoir characteristics. Therefore, a mapping relationship exists between the seismic waveforms and well-logging properties, which can be used to predict well-logging properties. This is the basis for predicting the well-logging properties constrained by seismic waveform clustering. In this study, we proposed a robust workflow for lithium brine prediction with the first application of well-logging property prediction constrained by waveform clustering using 3D seismic and well log data. Waveform clustering analysis based on the SVD algorithm is a matrix-based method with high computational efficiency and accuracy. This method can achieve clustering analysis of seismic waveforms, thereby realizing the partitioning of seismic faces. The number of effective samples is a parameter of the workflow. It is necessary to select a small amount of similar well data for the calculation, which affects the computational efficiency and accuracy of the process. Another important parameter is the optimal cutoff frequency. The well log data did not vary with changes in seismic waveforms over the entire frequency band, especially in the high-frequency region. Thus, it is necessary to distinguish between the low-frequency part that is controlled by seismic waveforms and the high-frequency part that is not controlled by seismic waveforms. This affected the resolution and reliability of the results, specifically the reliability of the results outside the seismic frequency band range. In practical applications, these two parameters must be comprehensively considered and determined using a correlation analysis.

The results in our study area indicate that the proposed workflow can accurately predict well-logging properties with high resolution. Compared with conventional neural network methods for predicting well-logging properties, the waveform-constrained method had evident geological significance. The prediction results of the high-quality reservoirs in our study area were verified by the elemental content test results, which demonstrated the effectiveness of the method. However, it was almost impossible to distinguish between the different elements in brines using seismic methods. This indicated that the same results may be obtained when brine contains other elements. Therefore, the elemental content test data in wells are important for controlling, and the more information there is, the more reliable the prediction results. This is one disadvantage of the proposed workflow. Incorporating geological genetic methods into this workflow is expected to enhance the reliability of the results, which will be the focus of future research.

Author Contributions: Conceptualization, Y.Z. and Y.Y.; methodology, Y.Y. and Z.W.; formal analysis, Z.W. and B.Z.; investigation, Z.W. and H.Z.; writing—review and editing, Y.Z., Y.Y. and H.Z.; supervision, Y.W. All authors have read and agreed to the published version of the manuscript.

Funding: This work was supported by the Natural Science Foundation of Sichuan Province (Grant Number 2022NSFSC1150).

Data Availability Statement: The data presented in this study are available on request from the corresponding author. The data are not publicly available because the company provided the data involving the commercial interests.

Acknowledgments: We would like to thank all the editors and three anonymous reviewers for their comments and helpful suggestions.

Conflicts of Interest: The authors declare no conflicts of interest.

References

1. He, M.-Y.; Luo, C.-G.; Yang, H.-J.; Kong, F.-C.; Li, Y.-L.; Deng, L.; Zhang, X.-Y.; Yang, K.-Y. Sources and a proposal for comprehensive exploitation of lithium brine deposits in the Qaidam Basin on the northern Tibetan Plateau, China: Evidence from Li isotopes. *Ore Geol. Rev.* **2020**, *117*, 103277. [CrossRef]
2. Bradley, D.C.; Stillings, L.L.; Jaskula, B.W.; Munk, L.A.; McCauley, A.D. Critical mineral resources of the United States—Economic and environmental geology and prospects for future supply. *Geol. Surv.* **2017**, *1802*, K1–K21.
3. Cabello, J. Lithium brine production, reserves, resources and exploration in Chile: An updated review. *Ore Geol. Rev.* **2021**, *128*, 103883. [CrossRef]
4. Liu, Y.; Tao, X.; Wang, Y.; Jiang, C.; Ma, C.; Sheng, O.; Lu, G.; Lou, X.W. Self-assembled monolayers direct a LiF-rich interphase toward long-life lithium metal batteries. *Science* **2022**, *375*, 739–745. [CrossRef] [PubMed]
5. Gil-Alana, L.A.; Monge, M. Lithium: Production and estimated consumption: Evidence of persistence. *Resour. Policy* **2019**, *60*, 198–202. [CrossRef]

6. Kesler, S.E.; Gruber, P.W.; Medina, P.A.; Keoleian, G.A.; Everson, M.P.; Wallington, T.J. Global lithium resources: Relative importance of pegmatite, brine and other deposits. *Ore Geol. Rev.* **2012**, *48*, 55–69. [CrossRef]
7. Christmann, P.; Gloaguen, E.; Labbé, J.F.; Jérémie, M.; Patrice, P. Global lithium resources and sustainability issues. In *Lithium Process Chemistry*; Elsevier: Amsterdam, The Netherlands, 2015; pp. 1–40.
8. Meng, F.; McNeice, J.; Zadeh, S.S.; Ghahreman, A. Review of lithium production and recovery from minerals, brines, and lithium-ion batteries. *Miner. Process. Extr. Metall. Rev.* **2021**, *42*, 123–141. [CrossRef]
9. Li, Q.; Wang, J.; Wu, C.; Fan, Q.; Qin, Z.; Chen, L.; Wei, H.; Du, Y.; Yuan, Q.; Li, J.; et al. Hydrochemistry and Sr-S isotope constraints on the source of lithium in the Nalenggele river and its terminal lakes, Qaidam basin. *Acta Geol. Sin.* **2021**, *95*, 2169–2182.
10. Gong, Y.; Liu, X.; Zhou, Q. Study on the composition and variation trend of oilfield brine in an oilfield of Jilin Province. *IOP Conf. Ser. Earth Environ. Sci.* **2020**, *592*, 012036.
11. Al-Thukair, A.A.; Ali, M.Y.; Al-Haddad, A.A.; Al-Zahrani, A.A.; Khan, S.A. Heavy metals distribution in the oilfield produced brine from the Al Khafji oilfield, Saudi Arabia. *J. Environ. Sci. Health A* **2013**, *48*, 393–399.
12. Moosavi, V.; Kazemi, G.A. Lithium recovery from oilfield-produced brines: A comprehensive review. *J. Petrol. Sci. Eng.* **2020**, *184*, 106698.
13. Yang, Y.; Lu, J.; Wang, Y. Separation of split shear waves based on a hodogram analysis of HTI media. *Acta Geophys.* **2018**, *66*, 643–658. [CrossRef]
14. Yi, J.; Bao, H.; Zheng, A.; Zhang, B.; Shu, Z.; Li, J.; Wang, C. Main factors controlling marine shale gas enrichment and high-yield wells in South China: A case study of the Fuling shale gas field. *Mar. Petrol. Geol.* **2019**, *103*, 114–125. [CrossRef]
15. Wen, H.; Wen, L.; Chen, H.; Zheng, R.; Dang, L.; Li, Y. Geochemical characteristics and diagenetic fluids of dolomite reservoirs in the Huanglong Formation, Eastern Sichuan Basin, China. *Petrol. Sci.* **2014**, *11*, 52–66. [CrossRef]
16. Ni, Y.; Zou, C.; Cui, H.; Li, J.; Lauer, N.E.; Harkness, J.S.; Kondash, A.J.; Coyte, R.M.; Dwyer, G.S.; Liu, D.; et al. Origin of flowback and produced waters from Sichuan Basin, China. *Environ. Sci. Technol.* **2018**, *52*, 14519–14527. [CrossRef] [PubMed]
17. Zhao, W.; Xu, C.; Wang, T.; Wang, H.; Wang, Z.; Bian, C.; Li, X. Comparative study of gas accumulations in the Permian Changxing reefs and Triassic Feixianguan oolitic reservoirs between Longgang and Luojiazhai-Puguang in the Sichuan Basin. *Chin. Sci. Bull.* **2011**, *56*, 3310–3320. [CrossRef]
18. Araoka, D.; Kawahata, H.; Takagi, T.; Watanabe, Y.; Nishimura, K.; Nishio, Y. Lithium and strontium isotopic systematics in playas in Nevada, USA: Constraints on the origin of lithium. *Miner. Depos.* **2014**, *49*, 371–379. [CrossRef]
19. Orberger, B.; Rojas, W.; Millot, R.; Flehoc, C. Stable isotopes (Li, O, H) combined with brine chemistry: Powerful tracers for Li origins in salar deposits from the Puna Region. *Procedia Earth Planet. Sci.* **2015**, *13*, 307–311. [CrossRef]
20. Zhang, B.; Liu, W.; Yang, K.; Pei, W.B.; Zhang, S.M.; Xiao, W. Salt accumulation, potassium formation mechanism and enrichment model of Triassic in northeast Sichuan Basin. *Earth Sci.* **2022**, *47*, 15–26.
21. Yu, X.C.; Liu, C.L.; Wang, C.L.; Xu, H.M.; Zhao, Y.J.; Huang, H.; Li, R.Q. Genesis of lithium brine deposits in the Jianghan Basin and progress in resource exploration: A review. *Earth Sci. Front.* **2022**, *29*, 107. [CrossRef]
22. Jiao, P.; Liu, C.; Bai, D.; Wang, M.; Chen, Y. Application of self-potential technique to the exploration of potassium-rich brine in Lop Nur, Xinjiang. *Acta Geosci. Sin.* **2005**, *26*, 381–385.
23. Yan, J.G.; Hou, L.; Zhao, Y.H.; Yang, X.Y. Application of seismic exploration method in east sichuan deep-seated potassium-rich brine exploration. *Eng. Sci.* **2013**, *15*, 59–65.
24. Huang, H.; Liu, C.L.; Zhang, S.W.; Xu, H.M.; Ye, J.Z.; Wang, C.L.; Peng, W.; Wen, H. Application of geophysical detection method to exploration of deep potassium rich brine formation: A case study of Jiangling depression. *Miner. Depos.* **2014**, *33*, 1101–1107.
25. Hou, X.H.; Feng, L.; Zheng, M.P.; Wang, W.; Fan, F.; Zhao, W.Y.; Gao, X.F. Recognition method of potassium-rich lithium brine reservoir in Nanyishan. *Earth. Sci.* **2022**, *47*, 45–55.
26. Smith, G.; Gidlow, P. Weighted stacking for rock property estimation and detection of gas. *Geophys. Prospect.* **1987**, *35*, 993–1014. [CrossRef]
27. Ruiz, F.; Cheng, A. A rock physics model for tight gas sand. *Lead. Edge* **2010**, *29*, 1484–1489. [CrossRef]
28. Lu, J.; Meng, X.; Wang, Y.; Yang, Z. Prediction of coal seam details and mining safety using multicomponent seismic data: A case history from China. *Geophysics* **2016**, *81*, B149–B165. [CrossRef]
29. Yang, Y.; Lu, J.; Li, H.; Qi, Q.; Zhou, H. Fracture prediction based on walkaround 3D3C vertical seismic profiling data: A case study from the Tarim Basin in China. *Geophysics* **2022**, *87*, D123–D136. [CrossRef]
30. Khoshdel, H.; Javaherian, A.; Saberi, M.R.; Varnousfaderani, S.R.; Shabani, M. Permeability estimation using rock physics modeling and seismic inversion. *J. Petrol. Sci. Eng.* **2022**, *219*, 111128. [CrossRef]
31. Keys, R.G.; Xu, S. An approximation for the Xu-White velocity model approximation for the Xu-White model. *Geophysics* **2002**, *67*, 1406–1414. [CrossRef]
32. Mavko, G.; Mukerji, T.; Dvorkin, J. *The Rock Physics Handbook: Tools for Seismic Analysis of Porous Media*; Cambridge University Press: Cambridge, UK, 2003.
33. Dvorkin, J.; Nur, A. Elasticity of high-porosity sandstones: Theory for two North Sea data sets. *Geophysics* **1996**, *61*, 1363–1370. [CrossRef]

34. Ruiz, F.; Azizov, I. Tight shale elastic properties using the soft-porosity and single aspect ratio models. In Proceedings of the 2011 SEG Annual Meeting, San Antonio, TX, USA, 18–23 September 2011; Expanded Abstracts of 81st Annual International SEG Meeting; pp. 2241–2245.
35. Xu, S.; White, R.E. A new velocity model for clays and mixtures. *Geophys. Prospect.* **1995**, *43*, 91–118. [CrossRef]
36. Xu, S.; Payne, M.A. Modeling elastic properties in carbonate rocks. *Lead. Edge* **2009**, *28*, 66–74. [CrossRef]
37. Schoenberg, M.; Sayers, C.M. Seismic anisotropy of fractured rock. *Geophysics* **1995**, *60*, 204–211. [CrossRef]
38. Bakulin, A.; Grechka, V.; Tsvankin, I. Estimation of fracture parameters from reflection seismic data—Part 1: HTI model due to a single fracture set. *Geophysics* **2000**, *65*, 1788–1802. [CrossRef]
39. Cooke, D.A.; Schneider, W.A. Generalized linear inversion of reflection seismic data. *Geophysics* **1983**, *48*, 665–676. [CrossRef]
40. Russell, B.; Hampson, D. Comparison of poststack seismic inversion methods. In *SEG Technical Program Expanded Abstracts*; Society of Exploration Geophysicists: Houston, TX, USA, 1991; pp. 876–878.
41. Kumar, R.; Das, B.; Chatterjee, R.; Sain, K. A methodology of porosity estimation from inversion of post-stack seismic data. *J. Nat. Gas Sci. Eng.* **2016**, *28*, 356–364. [CrossRef]
42. Aki, K.; Richards, P.G. *Quantitative Seismology*; W. H. Freeman & Co.: New York, NY, USA, 1980.
43. Zong, Z.; Li, K.; Yin, X.; Zhu, M.; Du, J.; Chen, W.; Zhang, W. Broadband seismic amplitude variation with offset inversion. *Geophysics* **2017**, *82*, M43–M53. [CrossRef]
44. Zong, Z.; Yin, X.; Yin, X.; Wu, G. Fluid identification method based on compressional and shear modulus direct inversion. *Chin. J. Geophys.* **2012**, *55*, 284–292. [CrossRef]
45. Lu, J.; Yang, Z.; Wang, Y.; Shi, Y. Joint PP and PS AVA seismic inversion using exact Zoeppritz equations. *Geophysics* **2015**, *80*, R239–R250. [CrossRef]
46. Lu, J.; Wang, Y.; Chen, J.; An, Y. Joint anisotropic amplitude variation with offset inversion of PP and PS seismic data. *Geophysics* **2018**, *83*, N31–N50. [CrossRef]
47. Liu, Z.; Liu, J. Seismic-controlled nonlinear extrapolation of well parameters using neural networks. *Geophysics* **1998**, *63*, 2035–2041. [CrossRef]
48. Torres, A.; Reveron, J.; Infant, J. Lithofacies discrimination using support vector machines, rock physics and simultaneous seismic inversion in clastic reservoirs in the Orinoco Oil Belt, Venezuela. In Proceedings of the 2013 SEG Annual Meeting, Houston, TX, USA, 22–27 September 2013.
49. Cheng, Y.; Fu, L.-Y. Nonlinear seismic inversion by physics-informed Caianiello convolutional neural networks for overpressure prediction of source rocks in the offshore Xihu depression, East China. *J. Petrol. Sci. Eng.* **2022**, *215*, 110654. [CrossRef]
50. Wu, M.; Fu, L.; Li, W. A high-resolution nonlinear inversion method of reservoir parameters and its application to oil/gas exploration. *Chin. J. Geophys.* **2008**, *51*, 386–399.
51. GiGiraud, J.; Pakyuz-Charrier, E.; Jessell, M.; Lindsay, M.; Martin, R.; Ogarko, V. Uncertainty reduction through geologically conditioned petrophysical constraints in joint inversion. *Geophysics* **2017**, *82*, ID19–ID34. [CrossRef]
52. Mosser, L.; Dubrule, O.; Blunt, M.J. Stochastic seismic waveform inversion using generative adversarial networks as a geological prior. *Math. Geosci.* **2020**, *52*, 53–79. [CrossRef]
53. Yao, F.; Gan, L. Application and restriction of seismic inversion. *Pet. Explor. Dev.* **2000**, *27*, 53–56.
54. Yin, X.; Cao, D.; Wang, B.; Zong, Z. Research progress of fluid discrimination with pre-stack seismic inversion. *Oil Geophys. Prospect.* **2014**, *49*, 22–34+46.
55. Pan, H.; Li, H.; Grana, D.; Zhang, Y.; Liu, T.; Geng, C. Quantitative characterization of gas hydrate bearing sediment using elastic-electrical rock physics models. *Mar. Petrol. Geol.* **2019**, *105*, 273–283. [CrossRef]
56. Yu, Z.; Wang, Z.; Lin, W.; Wang, J. Permeability prediction of tight conglomerates by integrating fractal characteristics and seismic meme inversion: A case study from the Triassic Baikouquan Formation, Junggar Basin, Western China. *Fractals* **2023**, *31*, 2340010. [CrossRef]
57. Chen, Y.; Bi, J.; Qiu, X.; Chen, Y.; Yang, H.; Cao, J.; Di, Y.; Zhao, H.; Li, Z. A method of seismic meme inversion and its application. *Pet. Explor. Dev.* **2020**, *47*, 1235–1245. [CrossRef]
58. Clavier, C.; Coates, G.; Dumanoir, J. Theoretical and experimental bases for the dual-water model for interpretation of shaly sands. *Soc. Petrol. Eng. J.* **1984**, *24*, 153–168. [CrossRef]
59. Atlas, W. *Introduction to Wireline Log Analysis*; Western Atlas International Inc.: Houston, TX, USA, 1995.
60. Archie, G.E. The electrical resistivity log as an aid in determining some reservoir characteristics. *Trans. AIME* **1942**, *146*, 54–62. [CrossRef]
61. Golub, G.; Loan, C. *Matrix Computations*; Johns Hopkins University Press: Baltimore, MD, USA, 2013. [CrossRef]
62. Hartigan, J.A.; Wong, M.A. Algorithm AS 136: A k-means clustering algorithm. *J. R. Stat. Soc. Ser. Appl. Stat.* **1979**, *28*, 100–108. [CrossRef]
63. Zhu, D.; Gibson, R. Seismic inversion and uncertainty quantification using transdimensional Markov chain Monte Carlo method. *Geophysics* **2018**, *83*, R321–R334. [CrossRef]
64. de Figueiredo, L.P.; Grana, D.; Roisenberg, M.; Rodrigues, B.B. Multimodal Markov chain Monte Carlo method for nonlinear petrophysical seismic inversion. *Geophysics* **2019**, *84*, M1–M13. [CrossRef]

65. Gu, Y.; Jiang, Y.; Fu, Y.; Chen, Z.; Zhang, J.; Zhou, L.; Jiang, Z. Hydrocarbon accumulation and main controlling factors of reef-shoal gas reservoirs in Changxing Formation in the complex tectonic area, eastern Sichuan Basin. *Arab. J. Geosci.* **2019**, *12*, 776–788. [CrossRef]
66. Huang, X. The Enrichment Regularity of Triassic Potassium—Rich Brines of the Salt—Bearing Sichuan Basin. Ph.D Thesis, China University of Geosciences, Beijing, China, 2013. (In Chinese with English Abstract).
67. Li, R.-Q.; Liu, C.-L.; Jiao, P.-C.; Wang, J.-Y. The tempo-spatial characteristics and forming mechanism of Lithium-rich brines in China. *China Geol.* **2018**, *1*, 72–83. [CrossRef]
68. Fu, L.Y. Application of the Caianiello neuron-based network to joint inversion. In *SEG Technical Program Expanded Abstracts*; Society of Exploration Geophysicists: Houston, TX, USA, 1997; pp. 1624–1627.